# Unveiling the Origin of Catalytic Sites of Pt Nanoparticles Decorated on Oxygen-Deficient Vanadium-Doped Cobalt Hydroxide Nanosheet for Hybrid Sodium–Air Batteries

Yao Kang,[†,○] Shuo Wang,[†,○] Yanyu Liu,[‡,○] Kwan San Hui,[*,§] Hai-feng Li,[†] Kar Wei Ng,[†] Feng Liang,[*,∥] Jianxin Geng,[⊥] Xiaoting Hong,[#] Wei Zhou,[*,▽] Kwun Nam Hui[*,†]

[†] Joint Key Laboratory of the Ministry of Education, Institute of Applied Physics and Materials Engineering, University of Macau, Avenida da Universidade, Taipa 999078, Macau SAR, China

[‡] School of Aerospace Engineering, Beijing Institute of Technology, Beijing 100081, China

[§] School of Engineering, University of East Anglia, Norwich NR4 7TJ, UK

[∥] State Key Laboratory of Complex Nonferrous Metal Resources Clean Utilization, Kunming University of Science and Technology, Kunming 650093, China

[⊥] Beijing Advanced Innovation Center for Soft Matter Science and Engineering, Beijing University of Chemical Technology, Beijing 100029, China

[#] Department of Chemistry, Zhejiang Sci-tech University, Hangzhou, 310018, PR China

[▽] Department of Physics, Tianjin Key Laboratory of Low Dimensional Materials Physics and Preparing Technology, School of Science, Tianjin University, Tianjin 300072, China

[○] These authors contributed equally

* Corresponding author

K. S. Hui, E-mail: k.hui@uea.ac.uk F. Liang, E-mail: liangfeng@kust.edu.cn

W. Zhou, E-mail: weizhou@tju.edu.cn K. N. Hui, E-mail: bizhui@um.edu.mo

**Abstract**

Highly active bifunctional electrocatalysts are crucial for improving the performance of rechargeable metal–air batteries. However, most reported bifunctional electrocatalysts feature poor electrocatalytic activity and stability toward oxygen reduction reaction (ORR) and oxygen evolution reaction (OER). Here, we have reported the first ever study of an effective one-step reduction-assisted exfoliation method to exfoliate bulk vanadium-doped cobalt hydroxide (V-doped $Co(OH)_2$, denoted as V-$Co(OH)_2$) into ultrathin nanosheets with abundant oxygen vacancies (V-$Co(OH)_2$-$O_v$) and simultaneously anchor them with highly dispersed ultrafine Pt nanoparticles (NPs) with nominal size of 0.8–2.4 nm (denoted as Pt/V-$Co(OH)_2$-$O_v$). The Pt/V-$Co(OH)_2$-$O_v$ catalyst exhibits improved catalytic performance in ORR/OER. X-ray absorption spectroscopy analysis and theoretical calculations reveal the strong interfacial electronic interactions between Pt NPs and V-$Co(OH)_2$-$O_v$, which synergistically improves oxygen intermediates adsorption/desorption, enhancing the ORR and OER performance. Using the Pt/V-$Co(OH)_2$-$O_v$ as a catalyst in the air cathode, a hybrid sodium–air battery displays a record value of ultralow charging-discharging voltage gap of 0.07 V at a current density of 0.01 mA $cm^{-2}$ with remarkable stability of up to 1000 cycles. This reduction-assisted exfoliation approach provides a new strategy to generate oxygen vacancies in metal hydroxides, which act as anchoring sites for deposition of sub-nano metal NPs via a strong interfacial effect.

***Keywords***: *vanadium-doped cobalt hydroxide, Pt nanoparticles, electronic structure reformation, DFT calculation, electrocatalysis, hybrid sodium-air battery*

## Introduction

With the rapid development of electric vehicles, developing low cost, high energy density, and long cycle life batteries has drawn significant attention from researchers in academia and industry.[1-3] Among rechargeable metal-air batteries, hybrid sodium-air batteries (HSABs) have been intensely considered as promising next-generation high-energy batteries because of low cost, high safety and environmental friendliness, exceeding the stored energy of the-state-of-art Li-ion batteries.[4] In 2013, K. Hayashi has first reported the development of an alkaline HSAB,[4] addressing the challenges of conventional sodium-air and lithium-oxygen batteries, that exhibits an electrochemical discharge capacity of 600 mAh $g^{-1}$, energy density of 1500 Wh $kg^{-1}$ and a maximum areal output power of 11 mW $cm^{-2}$. In theory, an alkaline HSAB can achieve a standard cell voltage of 3.11 V and a high specific capacity of 838 mAh $g^{-1}$ (2600 Wh $kg^{-1}$). However, ORR/OER usually involves multiple steps with one electron transfer per step, leading to sluggish kinetics with high discharge/charge overpotentials to overcome.[5-8] To date, platinum (Pt) and iridium oxide ($IrO_2$) or ruthenium oxide ($RuO_2$) are well-recognized electrocatalysts with favorable rates for ORR and OER, respectively.[9, 10] However, the high cost, scarcity, and unsatisfactory durability impede their widespread applications in alkaline metal–air batteries. Therefore, developing efficient bifunctional electrocatalysts to address the critical challenges of the electrocatalysts for the air cathodes in HSABs is urgently required, but still remains challenging.

Recently, low-cost transition metal (Co, Fe, and Ni)-based hydroxides have been demonstrated as promising electrocatalysts for OER because their 3d electronic structure could be modulated to weaken or strengthen the $OH^-$ adsorption energy.[11-17] Modulating the electronic structure of the metal center by dopants can be an effective method to enable favorable energetics for OER intermediates (*OH, *O, and *OOH) on the active sites[18, 19] and lowering the energy barrier of the rate-determining step (RDS) during OER.[20] In addition, generating oxygen vacancies in metal-doped transition metal hydroxides remarkably enhances the OER catalytic performance,[21-23] owing to the regulated electronic properties of the catalysts that facilitated high chemical reactivity of metal atoms for fast and efficient faradaic reactions.[23-25] However, the origin of the observed synergy among the metal dopant, the metal center and the oxygen vacancies as active sites for OER is yet to be further elucidated, that can provide significant insights into the rational design of efficient electrocatalysts.

Pt coupling with metal oxides, such as CoO,[26] $Ti_{0.7}Mo_{0.3}O_2$,[27] $ZrO_2$[28], and $TaB_2$[29], is a promising approach to enhance bifunctional catalytic activity and durability of the ORR/OER catalysts, that is attributed to the electronic interfacial effects of the heterojunction between two components.[30] Density functional theory (DFT) studies revealed that foreign metal nanoparticles (NPs) anchored on the catalyst substrate can effectively regulate the electron structure of active sites by taking advantage of the strong interfacial effect and synergistic catalytic characteristics of the NPs and catalyst substrate. As a result, the Gibbs formation energy required for active metal sites to reach the desired high oxidation state of compounds decreases, thus improving the

electrochemical activity.[30, 31] These studies suggest that the rational design and synthesis of heterogeneous bifunctional electrocatalysts by the combination of Pt NPs and metal-doped transition metal hydroxides with oxygen vacancies can lead to a highly active bifunctional electrocatalysts for rechargeable metal–air batteries. However, an in situ facile growth of such bifunctional electrocatalysts is still challenging.

Here, we reported an one-step reduction-assisted exfoliation approach to synthesize highly dispersed ultrafine Pt NPs (2.4 wt%) with nominal size of 0.8–2.4 nm on the ultrathin vanadium-doped cobalt hydroxide (V-doped $Co(OH)_2$) with abundant oxygen vacancies (denoted as Pt/V-$Co(OH)_2$-$O_v$) as an electrocatalyst for ORR/OER in alkaline solution. The Pt/V-$Co(OH)_2$-$O_v$ catalyst exhibited a low ORR onset potential ($\eta_{onset}$=0.91 V), low OER overpotential at a current density of 10 mA $cm^{-2}$ ($\eta_{10}$=145 mV), and small OER Tafel slope (62.8 mV $dec^{-1}$) in 1 M KOH, which are notably better than those of the pristine V-$Co(OH)_2$ and the V-$Co(OH)_2$-$O_v$. The improved catalytic activity of Pt/V-$Co(OH)_2$-$O_v$ is attributed to the increased valence state of neighboring Co and V atoms and the transfer of electron charge density from O to Co and V atoms, as evidenced from the X-ray absorption spectra. A HSAB was assembled using the Pt/V-$Co(OH)_2$-$O_v$ as the catalyst in the air electrode in an enclosed $O_2$-saturated 0.1 M NaOH system, displaying an extremely low charging-discharging voltage gap of 0.07 V at a current density of 0.01 mA $cm^{-2}$ and remarkable cycling stability of up to 1000 cycles.

## Results and discussion

### Exfoliation mechanism of V-$Co(OH)_2$ materials

In this study, V-$Co(OH)_2$ bimetal hydroxides were selected as starting materials owing to their high OER activity.[13] Figure 1 illustrates the synthesis of Pt/V-$Co(OH)_2$-$O_v$ via the reduction-assisted exfoliation of V-$Co(OH)_2$ in $NaBH_4$ solution. The layered structure of V-$Co(OH)_2$ can be easily intercalated by $H_2O$ and $BH_4^-$ molecules.[13] During stirring, $H_2$ bubbles were generated by the reaction of $H_2O$ with $NaBH_4$ (Eq. 1). $BH_4^-$ chemically destroyed the ionic and hydrogen bonds in the interlayers of the layered structure of V-$Co(OH)_2$, thus disturbing the normal charge balance and separating the positively charged brucite-like host layers from each other through the generated $H_2$ bubbles. Meanwhile, $NaBH_4$ induced the reduction etching of covalent bonds in the V-$Co(OH)_2$ host layers, which facilitated the escape of surface atoms from the lattice, the generation of multiple oxygen vacancies ($O_v$), and hence the subsequent formation of V-$Co(OH)_2$-$O_v$ (Eq. 1).[32] Simultaneously, Pt NPs were deposited on the abundant oxygen vacancy defects, acting as anchoring sites, on V-$Co(OH)_2$-$O_v$ nanosheet during stirring by the reduction with $NaBH_4$. Exfoliating layered structure materials to their 2D ultrathin nanosheets not only enables the exposure of nearly all surfaces with abundant catalytic active sites for lattice oxygen oxidation mechanism,[17] unlike 3D structured oxides that only allow the surface formation of O–O bonds,[33, 34] but also decreases the diffusion paths of ions.[35] Therefore, the as-exfoliated ultrathin Pt/V-$Co(OH)_2$-$O_v$ nanosheets featured porous ultrathin nanosheets with abundant oxygen vacancies, promoting essential electronic properties.[36] Importantly, in comparison with hydrothermal exfoliations, a reduction-assisted exfoliation is a clean, time-saving, non-

toxic method that requires no excess energy nor complicated manipulation with heat treatment and plasma.

$$2BH_4^- (aq) + 8OH^- (aq) \rightarrow B(OH)_4^- (aq) + BO_2^- (aq) + 2H_2O (l) + 4H_2 (g) + 8e^- \quad (1)$$

**Characterizations of materials**

The X-ray diffraction (XRD) patterns of V-$Co(OH)_2$ and V-$Co(OH)_2$-$O_v$ (Figure S1, Supporting Information) showed two main diffraction peaks at 33.8° and 59.9°, which can be indexed to the (012) and (110) planes of α-$Co(OH)_2$ (JCPDS 46-0605, trigonal crystal system, space group P-3m1, cell parameters a = 11.96 Å, b=6.36Å, c=25.00 Å, α=ß=γ=90°), respectively.[37] No other peak was observed, suggesting that a similar crystal structure was preserved before and after exfoliation. The morphology and ultrathin structures of the as-prepared samples were investigated via scanning electron microscopy (SEM). As shown in Figure S2 (a–f, Supporting Information), V-$Co(OH)_2$ without $NaBH_4$ treatment possessed a bulk and thick plate, whereas V-$Co(OH)_2$-$O_v$ exhibited a porous structure and ultrathin nanosheet features, indicating the successful reduction-assisted exfoliation of V-$Co(OH)_2$ bulk. Atomic force microscopy (AFM) showed that V-$Co(OH)_2$-$O_v$ ultrathin nanosheets measured ~3 nm in thickness (Figure 2a–b), whereas a thickness of over 20 nm was observed for the pristine V-$Co(OH)_2$ bulk (Figure S3, Supporting Information), confirming the role of $NaBH_4$ in the exfoliation of V-$Co(OH)_2$ bulk. The transmission electron microscopy (TEM) images of bulk V-$Co(OH)_2$ further confirmed the NP-like feature of the un-exfoliated V-$Co(OH)_2$ (Figure S4a, Supporting Information), whereas the reduction-assisted exfoliated V-$Co(OH)_2$-$O_v$

presented an ultrathin porous nanosheet structure (Figure S4b, Supporting Information). High-resolution TEM (HRTEM) images showed that the $NaBH_4$ reduction-assisted exfoliation of V-$Co(OH)_2$-$O_v$ involved 3–4 monolayers of V-$Co(OH)_2$ structure (Figure S5, Supporting Information), further demonstrating the successful exfoliation of bulk V-$Co(OH)_2$ materials. The HRTEM image and the selected area electron diffraction (SAED) pattern of V-$Co(OH)_2$ presented its polycrystal nature (Figure S6, Supporting Information), which is consistent with the XRD pattern (Figure S1, Supporting Information). The HRTEM image of V-$Co(OH)_2$-$O_v$ (Figure 2c) and its SAED (inset of Figure 2c) also revealed a polycrystal structure with two planes (102) and (110), caused by the partial etching of V-$Co(OH)_2$ by $NaBH_4$ during reduction-assisted exfoliation.[38] A magnified view of the HRTEM images (Figure 2d) showed disordered lattice stripes and atomic fluctuations in the V-$Co(OH)_2$-$O_v$ that might attribute to oxygen vacancies. The high-angle annular dark-field scanning TEM (HAADF-STEM) image and corresponding mapping images from energy-dispersive X-ray spectroscopy (EDS) indicated the homogeneous distribution of Co, V, and O in the whole nanosheet (Figures 2b–e). According to the EDS analysis (Figure S7f–g, Supporting Information), the composition ratio of Co:V was 3:1, in accordance with the feeding ratio. The HAADF-STEM image of Pt/V-$Co(OH)_2$-$O_v$ shows that ultrafine Pt NPs were uniformly distributed on the surface of V-$Co(OH)_2$-$O_v$, whereas the inset shows the particle size distribution plot (Figure 2i). The average size of Pt NPs is ~1.7 nm, which is smaller than that of Pt NPs synthesized via traditional impregnation–chemical reduction methods.[39] The TEM image (Figure 2j) further revealed that the deposited Pt NPs were homogeneously dispersed on the V-$Co(OH)_2$-$O_v$ without evident aggregation. Notably,

Pt NPs and V-$Co(OH)_2$-$O_v$ were embedded with each other, suggesting the matching nano-interfaces between the two components, which could synergistically enhance the catalytic activity and durability of the prepared material. Furthermore, the HRTEM image (Figure 2k) revealed that several Pt NPs were dispersed on the V-$Co(OH)_2$-$O_v$ nanosheets with distinct crystal lattices. A neighboring interlayer distance of 0.23 nm was assigned to the (111) plane of Pt (Zone 1), whereas the distance of 0.27 nm corresponded to the (012) plane of V-$Co(OH)_2$-$O_v$ (Zone 2). Notable disordered lattice stripes and atomic fluctuations were also observed in Pt/V-$Co(OH)_2$-$O_v$, suggesting rich defect sites in Pt/V-$Co(OH)_2$-$O_v$ (Figure 2k). The SAED pattern of Pt/V-$Co(OH)_2$-$O_v$ (Figure S7a, Supporting Information) showed three diffraction rings corresponding to the (111) plane of Pt NPs and the (012) and (110) planes of V-$Co(OH)_2$-$O_v$ in Pt/V-$Co(OH)_2$-$O_v$. Elemental mapping further demonstrated the homogenous distribution of Pt, Co, V, and O throughout the nanosheet structure in Pt/V-$Co(OH)_2$-$O_v$ (Figures S7b–e, Supporting Information), verifying the uniform dispersion of Pt NPs anchored on V-$Co(OH)_2$-$O_v$. Approximately 2.4 wt% Pt was determined for the synthesized Pt/V-$Co(OH)_2$-$O_v$ based on EDS (Figures S7f–g, Supporting Information).

X-ray photoelectron spectroscopy (XPS) measurements of the samples were conducted to investigate the influences of surface properties of materials on catalytic activities of ORR and OER. Figures 3(a–c) show the valence states of cations and the existence of oxygen vacancies on V-$Co(OH)_2$, V-$Co(OH)_2$-$O_v$, and Pt/V-$Co(OH)_2$-$O_v$ samples. Figure 3a shows the O 1s spectra of V-$Co(OH)_2$, V-$Co(OH)_2$-$O_v$, and Pt/V-$Co(OH)_2$-$O_v$, which can be deconvoluted into three characteristic peaks of oxygen

atoms bound to metals (529.86 eV for O1), defect sites with low oxygen coordination (530.89 eV for O2), and surface-adsorbed oxygen (531.75 eV for O3). V-$Co(OH)_2$-$O_v$ and Pt/V-$Co(OH)_2$-$O_v$ showed a considerably higher O2 percentage than that of V-$Co(OH)_2$ material (Table S1, Supporting Information). The higher O2 percentage of Pt/V-$Co(OH)_2$-$O_v$ (62.5%) and V-$Co(OH)_2$-$O_v$ (54.7%) indicates the presence of more oxygen vacancies in the samples compared with V-$Co(OH)_2$ (34.9%), which can be explained by Eq. 1. To further demonstrate the presence of oxygen vacancies in V-$Co(OH)_2$-$O_v$ and Pt/V-$Co(OH)_2$-$O_v$, we studied three samples via Raman scattering spectroscopy (Figure S8, Supporting Information). For the three samples, the peaks located at 169, 317, and 646 can be indexed to the characteristic bending and stretching vibrations of α-$Co(OH)_2$, whereas the peak located at 801 $cm^{-1}$ corresponds to V-O vibration. Notably, the Raman spectra of the three samples are similar, confirming the same crystal structure. The observed Raman peaks gradually broadened, and the peak intensity decreased after exfoliation, corresponding to the formation of defects, such as oxygen vacancies and lattice disorder, in V-$Co(OH)_2$-$O_v$ and Pt/V-$Co(OH)_2$-$O_v$.[40]

The fine-scanned Co 2p spectra were fitted to investigate the valence states of Co atoms (Figure 3b). Two main peaks for Co $2p_{3/2}$ and Co $2p_{1/2}$ were located at 781.21 and 797.32 eV, accompanied by two shake-up satellite peaks at 786.6 and 803.1 eV, respectively. The fitted peaks for Co $2p_{3/2}$ include $Co^{3+}$ (~780.54 eV) and $Co^{2+}$ (~781.21 eV), revealing the coexistence of $Co^{2+}$ and $Co^{3+}$, respectively. Compared to V-$Co(OH)_2$, the valence state of Co were shifted from $Co^{3+}$ to $Co^{2+}$ due to the electron transfer from the O to Co atoms, while it was slightly shifted back to $Co^{3+}$ in Pt/V-$Co(OH)_2$-$O_v$ due

to electron transfer from Co to Pt (as discussed in the X-ray absorption fine-structure spectroscopy (XAFS)). Notably, the atomic ratios of $Co^{2+}/Co^{3+}$ for V-$Co(OH)_2$-$O_v$ and Pt/V-$Co(OH)_2$-$O_v$ are 1.90 and 1.82, respectively, whereas that for V-$Co(OH)_2$ was 1.23 (Table S2, Supporting Information). Previous studies reported that a high atomic ratio of $Co^{2+}/Co^{3+}$ may indicate relatively high oxygen vacancies.[41, 42] Interestingly, the atomic ratio of $Co^{2+}/Co^{3+}$ slightly decreased to 1.82 for Pt/V-$Co(OH)_2$-$O_v$ compared with that of V-$Co(OH)_2$-$O_v$, because the Pt NPs altered the valence state and charge density of the material due to the electron transfer of Co atoms to Pt[30], as discussed in the section on XAFS. Similarly, V 2p XPS (Figure 3c) showed the same phenomenon; it displayed binding energies of 516.78 eV and 524.0 eV with a spin-orbit splitting of 7.22 eV, corresponding to the mixed $V^{3+}/V^{4+}/V^{5+}$ phase.

Figure S9 (Supporting Information) shows the high-resolution Pt 4f XPS spectra of Pt/V-$Co(OH)_2$-$O_v$. The peaks located at 71.4 and 74.9 eV in Pt/V-$Co(OH)_2$-$O_v$ are assigned to Pt $4f_{7/2}$ and Pt $4f_{5/2}$, respectively. Both peaks slightly shifted to lower binding energies relative to those of the peaks of the commercial Pt/C,[43] indicating that the interfacial electronic interactions between Pt NPs and V-$Co(OH)_2$-$O_v$ occurred due to the electron transfer from Co and V to Pt atoms after decoration with Pt NPs. Notably, the electronic modulation of V-$Co(OH)_2$-$O_v$ induced by Pt NPs and the interfacial synergy between Pt NPs and the V-$Co(OH)_2$-$O_v$ support can improve the adsorption/desorption features of oxygen species (e.g., *OH and *OOH), thereby boosting the electrocatalytic properties of Pt NPs (to be discussed later).

X-ray absorption near-edge structure (XANES) spectra were analyzed to probe the valence state of Co and V in the samples. Figure 3d-e shows the Co K-edge XANES spectra for V-$Co(OH)_2$, V-$Co(OH)_2$-$O_v$, and Pt/V-$Co(OH)_2$-$O_v$ samples. All samples showed a low-intensity pre-edge shoulder (so-called "the pre-edge peak") at ~7711 eV, which is attributed to the electronic transition from Co 1s orbital to the 3d orbital.[44] The strong absorption peak at ~7726 eV for Co K-edge was due to the dipole transition of Co 1s orbital to the 4p orbital.[44] The absorption edge of Co K-edge for the as-prepared V-$Co(OH)_2$, V-$Co(OH)_2$-$O_v$, and Pt/V-$Co(OH)_2$-$O_v$ samples shifted to higher energy compared with commercial α-$Co(OH)_2$, illustrating that Co existed as $Co^{2+}/Co^{3+}$ bonded with oxygen in the three samples.[44, 45] The absorption edge of Co K-edge for V-$Co(OH)_2$-$O_v$ and Pt/V-$Co(OH)_2$-$O_v$ shifted to lower energy compared with V-$Co(OH)_2$, revealing the partial electron transfer from O atoms to the Co 3d orbitals due to oxygen vacancies.[13, 30] Notably, the absorption edge of Co K-edge of Pt/V-$Co(OH)_2$-$O_v$ shifted to higher energy compared with V-$Co(OH)_2$-$O_v$, indicating a slight electron transfer from Co to Pt[30] and resulting in the shift of Co to a higher valence state, which is in good agreement with XPS results. Figure 3f-g presents the absorption edge of V K-edge XANES spectra of the as-prepared V-$Co(OH)_2$, V-$Co(OH)_2$-$O_v$, and Pt/V-$Co(OH)_2$-$O_v$. An evident pre-edge peak at 5465–5475 eV was observed and assigned to dipole-forbidden transitions from V 1s core levels to 3d states due to the combination of strong 3d–4p mixing and the overlap of metal 3d orbitals with 2p orbitals of the surrounding O atoms,[46, 47] and the peak intensity is proportional to the unoccupied density of the 3d states.[48] Hence, the oxidation state of V is $V^{3+}/V^{4+}/V^{5+}$ in V-$Co(OH)_2$, V-$Co(OH)_2$-$O_v$,

and Pt/V-$Co(OH)_2$-$O_v$, and this result is attributed to the further orbital hybridization between the 3d orbitals of Co and 2p orbitals of oxygen,[44] which is in good agreement with XPS results. In comparison with V-$Co(OH)_2$, the intensity of the pre-edge peak of V K-edge XANES spectra slightly decreased for V-$Co(OH)_2$-$O_v$ and Pt/V-$Co(OH)_2$-$O_v$ (Figure 3f-g). This finding suggests the partial electron transfer from O 2p to the V 3d orbitals due to oxygen vacancies. In addition, the intensity of V K-edge peak in Pt/V-$Co(OH)_2$-$O_v$ slightly increased compared with V-$Co(OH)_2$-$O_v$, indicating a partial electron transfer from V to Pt atoms.[49]

**OER and ORR electrocatalytic activity**

The electrocatalytic OER properties of V-$Co(OH)_2$, V-$Co(OH)_2$-$O_v$, and Pt/V-$Co(OH)_2$-$O_v$ were examined by coating the samples on a glassy carbon (GC) electrode in a three-electrode configuration in 1 M KOH at a scan rate of 10 mV $s^{-1}$. As shown in Figure 4a, the performance of different catalysts varied from the anodic polarization currents recorded via linear sweep voltammetry (LSV). Remarkably, the Pt/V-$Co(OH)_2$-$O_v$ exhibited the highest OER catalytic activity with the lowest onset potential of 1.41 V compared with V-$Co(OH)_2$-$O_v$ (1.57 V), V-$Co(OH)_2$ (1.61 V), and Ir/C (1.62 V). Liu et al. reported that vanadium-doped cobalt hydroxide can significantly enhance the OER activity at the Co sites.[13] This improvement is attributed to the changes in $OH^-$ absorption Gibbs free energy ($\triangle G_{OH}$) and the $O^{2-}$-to-$OH^-$ absorption energy difference ($\triangle G_O - \triangle G_{OH}$), as rationalized by the difference in electron affinity between Co (63.7 kJ/mol) and V (50.6 kJ/mol) ions.[14, 50] For V-$Co(OH)_2$-$O_v$, the existence of V atoms could also lead to changes in $\triangle G_{OH}$ and $\triangle G_O - \triangle G_{OH}$ at the Co sites and

facilitate the formation of $OH^-$ and $O^{2-}$ intermediates on the surface $Co^{3+}$ neighboring the oxygen vacancy, thus promoting the OER activity.[14, 50] In particular, the Pt/V-$Co(OH)_2$-$O_v$ required an overpotential of 145 mV to reach a current density of 10 mA $cm^{-2}$, whereas the V-$Co(OH)_2$-$O_v$, V-$Co(OH)_2$, and Ir/C required 266, 321, and 420 mV, respectively. At a high current density of 50 mA $cm^{-2}$, Pt/V-$Co(OH)_2$-$O_v$ showed a lower overpotential of 432 mV compared with V-$Co(OH)_2$-$O_v$ (468 mV), V-$Co(OH)_2$ (520 mV), and Ir/C (542 mV). The electrochemical data illustrate that the Pt/V-$Co(OH)_2$-$O_v$ nanosheets showed improved electrocatalytic activity that is superior to those of most catalysts in literature (Table S4, Supporting Information).

Steady-state Tafel measurements were performed to evaluate the kinetics of materials; the results are presented in Figure 4b. Pt/V-$Co(OH)_2$-$O_v$ exhibited the smallest Tafel slope of 62.8 mV $decade^{-1}$ compared with V-$Co(OH)_2$-$O_v$ (75.9 mV $decade^{-1}$), V-$Co(OH)_2$ (90.6 mV $decade^{-1}$), and Ir/C (65.3 mV $decade^{-1}$), indicating superior kinetics for OER. To further study the electrode reaction kinetics, we conducted electrochemical impedance spectroscopy analysis and measured the electrochemical surface area (ECSA) of Pt/V-$Co(OH)_2$-$O_v$, V-$Co(OH)_2$-$O_v$, and V-$Co(OH)_2$ electrodes in a three-electrode configuration in 1 M KOH (Figure S10a, Supporting Information). The equivalent circuit (inset of Figure S10a, Supporting Information) comprised an electrolyte resistance ($R_s$) in series with a parallel combination of a constant phase element and a charge-transfer resistance ($R_{ct}$). The Nyquist diagrams of the three electrodes (Figure S10a, Supporting Information) show notable semicircles in the high-frequency range, which are mainly related to charge

transfer resistance in the catalyst. Nyquist plots revealed a dramatic decrease in $R_{ct}$ (3.5 Ω) for Pt/V-Co(OH)$_2$-O$_v$ compared with those of V-Co(OH)$_2$-O$_v$ (5.3 Ω) and V-Co(OH)$_2$ (6.4 Ω). The lowest value obtained suggests the rapid hydroxide ion transfer in the Pt/V-Co(OH)$_2$-O$_v$ electrode that promoted a high OER activity. This phenomenon is also reflected in the Bode plots (Figure S10b, Supporting Information), where Pt/V-Co(OH)$_2$-O$_v$ showed the smallest resistance in the tested frequency range compared with V-Co(OH)$_2$ and V-Co(OH)$_2$-O$_v$. The ECSA, related to the double-layer capacitances ($C_{dl}$) of different electrodes, were determined via cyclic voltammetry (CV). (Figure S11, Supporting Information). The $C_{dl}$ of Pt/V-Co(OH)$_2$-O$_v$ (177.2 mF cm$^{-2}$) is considerably higher than those of V-Co(OH)$_2$-O$_v$ (83.9 mF cm$^{-2}$) and V-Co(OH)$_2$ (4.7 mF cm$^{-2}$), indicating that Pt/V-Co(OH)$_2$-O$_v$ possessed a higher density of catalytic active sites. To evaluate the long-term stability of Pt/V-Co(OH)$_2$-O$_v$ toward OER, we recorded the LSV curves before and after 1000 accelerated CV cycles (Figure 4c). No apparent activity degradation was observed, indicating the outstanding durability of the electrode for OER electrocatalysis. In addition, chronoamperometric curves (Figure S12, Supporting Information) showed that Pt/V-Co(OH)$_2$-O$_v$ exhibited a substantially higher current retention (100%, 10,000 s) than the benchmark Ir/C, indicating the remarkable catalytic durability of Pt/V-Co(OH)$_2$-O$_v$.

The ORR catalytic performances of Pt/V-Co(OH)$_2$-O$_v$, V-Co(OH)$_2$-O$_v$, and V-Co(OH)$_2$ were investigated by coating the same mass of samples in a GC electrode in O$_2$-saturated 0.1 M KOH at a scan rate of 10 mV s$^{-1}$. As shown in Figures 4d-e, Pt/V-Co(OH)$_2$-O$_v$ exhibited the remarkably highest onset potential (0.91 V versus reversible

hydrogen electrode [RHE]) than V-$Co(OH)_2$-$O_v$ (0.70 V versus RHE) and V-$Co(OH)_2$ (0.65 V versus RHE), indicating that Pt/V-$Co(OH)_2$-$O_v$ achieved the best ORR catalytic performance. Similarly, Pt/V-$Co(OH)_2$-$O_v$ showed a higher half-wave potential of 0.82 V than V-$Co(OH)_2$-$O_v$ (0.65 V) and V-$Co(OH)_2$ (0.6 V), and this value is comparable to those of commonly reported catalysts (Table S5, Supporting Information). In addition, the limited current density reveals the efficient ORR performance of Pt/V-$Co(OH)_2$-$O_v$ (Figure 4e), which exhibited a current density of 5 mA $cm^{-2}$, which is higher than those of V-$Co(OH)_2$-$O_v$ (3 mA $cm^{-2}$) and V-$Co(OH)_2$ (2 mA $cm^{-2}$). LSV curves at different rotation speeds were investigated the electron transfer capability of the samples (Figure 4f), and the results were fitted using the Koutecký–Levich (K–L) plot. Based on the K–L equation, the calculated electron transfer number (*n*) of Pt/V-$Co(OH)_2$-$O_v$ is 3.81, implying its $4e^-$ transfer pathway for ORR. The *n* for V-$Co(OH)_2$-$O_v$ and V-$Co(OH)_2$ are 3.2 and 2.0 (Figure S13, Supporting Information), respectively, indicating their poor ORR performance.

**Mechanistic study on ORR and OER of materials**

To unveil the active site of Pt/V-$Co(OH)_2$-$O_v$ for ORR/OER, DFT calculations were carried out. First, we determined the optimal site for creating oxygen vacancy in V-$Co(OH)_2$ by calculating the oxygen vacancy formation energy in order to build the possible V-$Co(OH)_2$-$O_v$ slab model. In the V-$Co(OH)_2$ structure, two oxygen vacancy configurations were observed due to crystal symmetry (Figure S14a, Supporting Information). The calculation results indicated that the oxygen vacancies at site 2

resulted in a relatively higher oxygen vacancy formation energy (0.8 eV) than that at site 1 through the bonding of two Co atoms and one V atoms (Table S6, Supporting Information), suggesting that the formation of oxygen vacancy is more energetically favored in site 1. Thus, the slab model with oxygen vacancy at site 1 was selected in this work. In the presence of oxygen vacancies, four different adsorption sites for ORR and OER were considered (Figure S14b, Supporting Information). The adsorption energy at the oxygen vacancies of site I was the lowest due to the direct bonding of intermediates with exposed metal Co and V (Table S7, Supporting Information). As a result, for the V-$Co(OH)_2$-$O_v$ slab model, the existence of oxygen vacancies changed the active sites from oxygen atoms in V-$Co(OH)_2$ to the metal active sites (Co and V) in V-$Co(OH)_2$-$O_v$, signifying the changes in the active sites are a key factor in improving the ORR and OER performance as discussed below. Considering that the reaction free energy ($\Delta G$) is an important parameter for describing catalytic activities, $\Delta G$ was calculated to estimate the overpotential for ORR/OER. The magnitude of overpotential refers to the discrepancy in the RDS potential (maximum $\Delta G_n$ over the charge $e$) and the standard Nernstian potential (1.23 V vs. RHE). For the V-$Co(OH)_2$ model, the oxygen intermediates cannot be adsorbed on the surface oxygen in the vacuum layer (FigureS15, Supporting Information). This may be attributed to the passivated dimer oxygen at the adsorption site.[51, 52] Hence, it will not be considered for further analysis. In the case of V-$Co(OH)_2$-$O_v$, oxygen vacancies are the active sites (Figure S16 for the details of adsorbed structures) and the ORR limiting potential of 1.27 eV was observed at step iv (Figure 5c). In the Pt/V-$Co(OH)_2$-$O_v$ structure, Pt NPs

were anchored on the oxygen vacancies of V-Co$(OH)_2$-$O_v$ (denoted as Pt1/V-Co$(OH)_2$-$O_v$, Figure 5a), and Pt NPs anchored next to the oxygen vacancies of V-Co$(OH)_2$-$O_v$ (denoted as Pt2/V-Co$(OH)_2$-$O_v$, Figure S17, Supporting Information) were further studied to elucidate the active site for ORR/OER. The calculation results (Figure 5b) indicated that the Pt-top site of Pt1/V-Co$(OH)_2$-$O_v$ (-0.22 eV, step iv of Figure 5c) resulted in lower ORR limiting potential compared to that of Pt2/V-Co$(OH)_2$-$O_v$ (-0.20 V, step iv of Figure 5c).

The OER pathway is regarded as the reverse process of ORR. Figures 5b and 5d show the calculated $\Delta G_n$ for the V-Co$(OH)_2$-$O_v$, Pt1/V-Co$(OH)_2$-$O_v$ and Pt2/V-Co$(OH)_2$-$O_v$. For the V-Co$(OH)_2$-$O_v$ model, the theoretical results indicated that the surface vacancy site exhibited a limiting potential of 2.76 eV with the RDS of $O_2$ formation (step iv of Figure 5d and Table S8, Supporting Information). For the Pt2/V-Co$(OH)_2$-$O_v$, the theoretical limiting potential of OER slightly reduced to 2.38eV with the RDS of *OOH (step iii of Figure 5d). In the case of Pt1/V-Co$(OH)_2$-$O_v$, the RDS of *OOH (step iii of Figure 5d) further decreased to 2.20 eV. It is well-recognized that the key to a high ORR/OER activity is related to the stability of adsorbed *OOH, *OH and *O.[53, 54] Compared to the V-Co$(OH)_2$-$O_v$, Pt cluster anchored on the oxygen vacancy of V-Co$(OH)_2$-$O_v$ can weaken the adsorption strength of the oxygen intermediates on the Pt active site (Table S9, Supporting Information), leading toward lower energy barrier and thus higher reaction activity. Based on the DFT results, the Pt1/V-Co$(OH)_2$-$O_v$ was the preferred structure for ORR/OER activities and was considered for further study of the density of states (DOS).

To further explore the influence of Pt NPs and oxygen vacancies on the ORR/OER activity, we calculated the DOS of V-Co$(OH)_2$, V-Co$(OH)_2$-$O_v$, and Pt1/V-Co$(OH)_2$-$O_v$ (Figure S19, Supporting Information). The calculated DOS plots show the valence bands of both the up-spin and down-spin channels for V-Co$(OH)_2$, V-Co$(OH)_2$-$O_v$, and Pt1/V-Co$(OH)_2$-$O_v$ near the Fermi level, indicating the metallic character of materials. However, V-Co$(OH)_2$-$O_v$ and Pt1/V-Co$(OH)_2$-$O_v$ showed relatively low DOS at the Fermi level, indicating an efficient modulation of the electrical conductivity induced by oxygen vacancies. This condition occurred because delocalized electrons near the oxygen vacancies were easily excited into the conduction band, thus enhancing the conductivity and electrocatalytic activity of the catalyst.[50] As layered double hydroxides suffer from low electrical conductivity, in this study, the high electrical conductivity of Pt/V-Co$(OH)_2$-$O_v$ enhanced the charge transfer (Figure S11, Supporting Information), which is in good agreement with the low Tafel slope in Figure 4b. Compared to V-Co$(OH)_2$, oxygen vacancies in V-Co$(OH)_2$-$O_v$ lead to the lower valence state of metal atoms (Table S10, Supporting Information) due to delocalization of electrons near Co and V atoms. Thus, for V-Co$(OH)_2$-$O_v$, it is anticipated that the transfer of active sites from O atoms to metal atoms dominated the OER, improving the OER activity. Charge density difference (Figure S20, Supporting Information) shows that there is obvious charge accumulation around the Pt atoms neighboring Co and V atoms, indicating electron transfer from Co and V to Pt. The charge transfer from Co and V atoms to Pt atoms is further revealed by the increase of the valence state of Co and V atoms (Table S10, Supporting Information), which is

consistent with XPS and XANES results. The results further demonstrate the interfacial electronic interactions between Pt NPs and V-$Co(OH)_2$-$O_v$. Figure 5e shows the calculated electrostatic potential (ESP) of the Pt/V-$Co(OH)_2$-$O_v$ structures. The Pt clusters of Pt1/V-$Co(OH)_2$-$O_v$ and Pt2/V-$Co(OH)_2$-$O_v$ are blue, while the V-$Co(OH)_2$ substrates are yellow. The bluer the place, the higher the ESP (absence of electrons); it is easier to be attacked by nucleophilic reagent such as $OH^-$ ion, while the reddish place has a lower ESP (abundance of electrons) and is more susceptible to attack by electrophilic reagent such as $H^+$ ion. The DFT results are in agreement with the experimental study that Pt metal is the active site for ORR and OER.[53, 54] We speculate that the interfacial electronic interaction between Pt NPs active sites and V-$Co(OH)_2$-$O_v$ could effectively accelerate electron transfer rate, which not only facilitates the oxygen intermediates adsorption/desorption behaviors on Pt NPs active sites but also effectively reduces the energy barrier of rate-limiting step during the electrocatalytic process, thereby improving ORR and OER performance (Figure S20, Supporting information).

**Fabrication of HSAB based on the liquid anode and Pt/V-$Co(OH)_2$-$O_v$ as catalysts in air cathode**

To demonstrate the potential of the Pt/V-$Co(OH)_2$-$O_v$ electrocatalyst for actual applications, we fabricated a HSAB. The battery consisted of a liquid anode, a NASICON solid electrolyte as a separator, an $O_2$-saturated NaOH aqueous electrolyte, and the Pt/V-$Co(OH)_2$-$O_v$ catalysts in the air cathode (Figure 6a). During discharge,

$Na^+$ migrated to the catholyte, and $O_2$ was reduced to $OH^-$; this process differs from that of traditional sodium-air batteries.

Anode: Na 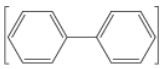 $\leftrightarrow$ 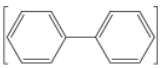 $+ \quad Na^+ + e^-$ (2)

Cathode: $4OH^- \leftrightarrow 2H_2O + O_2 + 4e^-$ (3)

The charge–discharge curves of HSABs based on the different cathodes are shown in Figure 6b, where ΔV denotes the gap between charge and discharge voltages. Pt/V-$Co(OH)_2$-$O_v$ exhibited the best performance with the lowest Δ*V* of 0.07 V at a current density of 0.01 mA $cm^{-2}$ compared with V-$Co(OH)_2$-$O_v$ (0.12 V) and V-$Co(OH)_2$ (0.29 V). The charge/discharge experiments verified the superiority of Pt/V-$Co(OH)_2$-$O_v$ among the prepared catalysts in the full-cell configuration. The round-trip efficiency (charge-to-discharge voltage ratio) of HSABs using Pt/V-$Co(OH)_2$-$O_v$ reached 97.3% compared with V-$Co(OH)_2$-$O_v$ (93.2%) and V-$Co(OH)_2$ (89.3%). The air cathode stability was examined by performing constant-current charge–discharge with up to 300 cycles. This process is crucial for the confirmation of the air cathode's potential for practical applications in rechargeable batteries. Figure 6c shows the charge–discharge profiles of the HSAB with Pt/V-$Co(OH)_2$-$O_v$ catalyst. No significant drop in potential was observed under continuous charge–discharge of the battery. No significant change nor decrease was observed in the discharge voltage for up to 1000 cycles (Figure 6d), indicating the reversibility of the battery. The roundtrip efficiency slightly dropped by 2.2% after 1000 cycles, which is a desirable value compared with those of other reported HSABs (Table S10, Supporting Information). This closed-system HSAB displayed significantly durable device performance in terms of voltage gap, roundtrip

efficiency, and cycling performances compared with previously reported HSABs. Furthermore, the power density of the HSAB delivered a maximum specific power density of 407 mW $g^{-1}$ (Figure 6e), which is the highest among the reported values for HSABs.

## Conclusion

In conclusion, a low-cost and effective one-step reduction-assisted exfoliation method was developed for exfoliating 3D bulk V-$Co(OH)_2$ into ultrathin nanosheets with numerous oxygen vacancies for anchoring of ultrafine Pt NPs. In comparison with the traditional liquid exfoliation, this method is a clean, time-saving, non-toxic, low-cost procedure that requires no additional energy. For the Pt/V-$Co(OH)_2$-$O_v$ sample, Pt NPs are the active sites for ORR/OER. A closed-system HASB was fabricated using the Pt/V-$Co(OH)_2$-$O_v$ catalyst in the air cathode, displaying an extremely low voltage gap of 0.07 V at a current density of 0.01 mA $cm^{-2}$, a remarkable cycling performance of up to 1000 cycles, and superior energy efficiency of 97.3%, which are better than those HSABs reported in literature. The reduction-assisted exfoliation approach provides a strategy for exfoliating 3D bulk materials to 2D materials with enhanced electrocatalytic properties, thus enabling the development of highly active heterogeneous electrocatalysts for energy storage and conversion applications.

## Acknowledgement

This work was funded by The Science and Technology Development Fund, Macau SAR (File no. 0191/2017/A3, 0041/2019/A1, 0046/2019/AFJ, 0021/2019/AIR), University

of Macau (File no. MYRG2017-00216-FST and MYRG2018-00192-IAPME), and the UEA funding. The DFT calculations were performed at High Performance Computing Cluster (HPCC) of Information and Communication Technology Office (ICTO) at University of Macau.

## References


1. Kang, Y.; Liang, F.; Hayashi, K. J. E. A., Hybrid Sodium–Air Cell with Na [FSA–C2C1im][FSA] Ionic Liquid Electrolyte. *Electrochim. Acta* **2016,** *218*, 119-124.

2. Liang, F.; Qiu, X. C.; Zhang, Q. K.; Kang, Y.; Koo, A.; Hayashi, K.; Chen, K. F.; Xue, D. F.; Hui, K. N.; Yadegari, H.; Sun, X. L., A liquid anode for rechargeable sodium-air batteries with low voltage gap and high safety. *Nano Energy* **2018,** *49*, 574-579.

3. Xu, X. L.; San Hui, K.; Dinh, D. A.; Hui, K. N.; Wang, H., Recent advances in hybrid sodium-air batteries. *Mater. Horizons* **2019,** *6* (7), 1306-1335.

4. Hayashi, K.; Shima, K.; Sugiyama, F., A Mixed Aqueous/Aprotic Sodium/Air Cell Using a NASICON Ceramic Separator. *J. Electrochem. Soc.* **2013,** *160* (9), A1467-A1472.

5. Hong, W. T.; Risch, M.; Stoerzinger, K. A.; Grimaud, A.; Suntivich, J.; Shao-Horn, Y., Toward the rational design of non-precious transition metal oxides for oxygen electrocatalysis. *Energy Environ. Sci.* **2015,** *8* (5), 1404-1427.

6. Shao, M.; Chang, Q.; Dodelet, J. P.; Chenitz, R., Recent Advances in Electrocatalysts for Oxygen Reduction Reaction. *Chem. Rev.* **2016,** *116* (6), 3594-657.

7. Dai, L.; Xue, Y.; Qu, L.; Choi, H. J.; Baek, J. B., Metal-free catalysts for oxygen reduction reaction. *Chem. Rev.* **2015,** *115* (11), 4823-4892.

8. Suen, N. T.; Hung, S. F.; Quan, Q.; Zhang, N.; Xu, Y. J.; Chen, H. M., Electrocatalysis for the oxygen evolution reaction: recent development and future perspectives. *Chem. Soc. Rev.* **2017,** *46* (2), 337-365.

9. Zhang, R. H.; Dubouis, N.; Ben Osman, M.; Yin, W.; Sougrati, M. T.; Corte, D. A. D.; Giaume, D.; Grimaud, A., A Dissolution/Precipitation Equilibrium on the Surface of Iridium-Based Perovskites Controls Their Activity as Oxygen Evolution Reaction Catalysts in Acidic Media. *Angew. Chem. Int. Ed.* **2019,** *58* (14), 4571-4575.

10. Yeo, B. S., Oxygen evolution by stabilized single Ru atoms. *Nat. Catal.* **2019,** *2* (4), 284-285.

11. Feng, J. X.; Ye, S. H.; Xu, H.; Tong, Y. X.; Li, G. R., Design and Synthesis of FeOOH/CeO2 Heterolayered Nanotube Electrocatalysts for the Oxygen Evolution Reaction. *Adv. Mater.* **2016,** *28* (23), 4698-4703.

12. Huang, J.; Chen, J.; Yao, T.; He, J.; Jiang, S.; Sun, Z.; Liu, Q.; Cheng, W.; Hu, F.; Jiang, Y.; Pan, Z.; Wei, S., CoOOH Nanosheets with High Mass Activity for Water Oxidation. *Angew. Chem. Int. Ed.* **2015,** *54* (30), 8722-8727.

13. Liu, J. Z.; Ji, Y. F.; Nai, J. W.; Niu, X. G.; Luo, Y.; Guo, L.; Yang, S. H., Ultrathin amorphous cobalt-vanadium hydr(oxy)oxide catalysts for the oxygen evolution reaction. *Energy Environ. Sci.* **2018,** *11* (7), 1736-1741.

14. Burke, M. S.; Kast, M. G.; Trotochaud, L.; Smith, A. M.; Boettcher, S. W., Cobalt-iron (oxy)hydroxide oxygen evolution electrocatalysts: the role of structure and composition on activity, stability, and mechanism. *J. Am. Chem. Soc.* **2015,** *137* (10), 3638-3648.

15. Xu, X.; Song, F.; Hu, X., A nickel iron diselenide-derived efficient oxygen-evolution catalyst. *Nat. Commun.* **2016,** *7*, 1-7.

16. Zhao, Y.; Jia, X.; Chen, G.; Shang, L.; Waterhouse, G. I.; Wu, L. Z.; Tung, C. H.; O'Hare, D.; Zhang, T., Ultrafine NiO Nanosheets Stabilized by TiO2 from Monolayer NiTi-LDH Precursors: An Active Water Oxidation Electrocatalyst. *J. Am. Chem. Soc.* **2016,** *138* (20), 6517-6524.

17. Sun, Y.; Gao, S.; Lei, F.; Xie, Y., Atomically-thin two-dimensional sheets for understanding active sites in catalysis. *Chem. Soc. Rev.* **2015,** *44* (3), 623-636.

18. Zhang, B.; Zheng, X.; Voznyy, O.; Comin, R.; Bajdich, M.; Garcia-Melchor, M.; Han, L.; Xu, J.; Liu, M.; Zheng, L.; Garcia de Arquer, F. P.; Dinh, C. T.; Fan, F.; Yuan, M.; Yassitepe, E.; Chen, N.; Regier, T.; Liu, P.; Li, Y.; De Luna, P.; Janmohamed, A.; Xin, H. L.; Yang, H.; Vojvodic, A.; Sargent, E. H., Homogeneously dispersed multimetal oxygen-evolving catalysts. *Science* **2016,** *352* (6283), 333-337.

19. Du, J.; Li, C.; Wang, X.; Shi, X.; Liang, H. P., Electrochemical Synthesis of Cation Vacancy-Enriched Ultrathin Bimetallic Oxyhydroxide Nanoplatelets for Enhanced Water Oxidation. *ACS Appl. Mater. Interfaces* **2019,** *11* (29), 25958-25966.

20. Niu, S.; Jiang, W. J.; Wei, Z.; Tang, T.; Ma, J.; Hu, J. S.; Wan, L. J., Se-Doping Activates FeOOH for Cost-Effective and Efficient Electrochemical Water Oxidation. *J. Am. Chem. Soc.* **2019,** *141* (17), 7005-7013.

21. Ling, T.; Yan, D. Y.; Jiao, Y.; Wang, H.; Zheng, Y.; Zheng, X.; Mao, J.; Du, X. W.; Hu, Z.; Jaroniec, M.; Qiao, S. Z., Engineering surface atomic structure of single-crystal cobalt (II) oxide nanorods for superior electrocatalysis. *Nat. Commun.* **2016,** *7*, 12876-12884.

22. Kim, J.; Yin, X.; Tsao, K. C.; Fang, S.; Yang, H., Ca(2)Mn(2)O(5) as oxygen-deficient perovskite electrocatalyst for oxygen evolution reaction. *J. Am. Chem. Soc.* **2014,** *136* (42), 14646-14659.

23. Xu, L.; Jiang, Q.; Xiao, Z.; Li, X.; Huo, J.; Wang, S.; Dai, L., Plasma-Engraved $Co_3O_4$ Nanosheets with Oxygen Vacancies and High Surface Area for the Oxygen Evolution Reaction. *Angew. Chem. Int. Ed.* **2016,** *55* (17), 5277-5281.

24. Song, F.; Hu, X., Exfoliation of layered double hydroxides for enhanced oxygen evolution catalysis. *Nat. Commun.* **2014,** *5*, 4477-4486.

25. Xiao, Z.; Wang, Y.; Huang, Y.-C.; Wei, Z.; Dong, C.-L.; Ma, J.; Shen, S.; Li, Y.; Wang, S., Filling the oxygen vacancies in $Co_3O_4$ with phosphorus: an ultra-efficient electrocatalyst for overall water splitting. *Energy Environ. Sci.* **2017,** *10* (12), 2563-2569.

26. Meng, C.; Ling, T.; Ma, T. Y.; Wang, H.; Hu, Z.; Zhou, Y.; Mao, J.; Du, X. W.; Jaroniec, M.; Qiao, S. Z., Atomically and Electronically Coupled Pt and CoO Hybrid Nanocatalysts for Enhanced Electrocatalytic Performance. *Adv. Mater.* **2017,** *29* (9), 1604607-1604614.

27. Ho, V. T.; Pan, C. J.; Rick, J.; Su, W. N.; Hwang, B. J., Nanostructured $Ti_{(0.7)}Mo_{(0.3)}O_2$ support enhances electron transfer to Pt: high-performance catalyst for oxygen reduction reaction. *J. Am. Chem. Soc.* **2011,** *133* (30), 11716-11724.

28. Wang, T. Y.; Nam, G.; Jin, Y.; Wang, X. Y.; Ren, P. J.; Kim, M. G.; Liang, J. S.; Wen, X. D.; Jang, H.; Han, J. T.; Huang, Y. H.; Li, Q.; Cho, J., NiFe (Oxy) Hydroxides Derived from NiFe Disulfides as an Efficient Oxygen

Evolution Catalyst for Rechargeable Zn-Air Batteries: The Effect of Surface S Residues. *Adv. Mater.* **2018,** *30* (27), 1800757-1800766.

29. Toyoda, E.; Jinnouchi, R.; Ohsuna, T.; Hatanaka, T.; Aizawa, T.; Otani, S.; Kido, Y.; Morimoto, Y., Catalytic activity of Pt/$TaB_2$(0001) for the oxygen reduction reaction. *Angew. Chem. Int. Ed.* **2013,** *52* (15), 4137-4140.

30. Han, X. P.; Wu, X. Y.; Deng, Y. D.; Liu, J.; Lu, J.; Zhong, C.; Hu, W. B., Ultrafine Pt Nanoparticle-Decorated Pyrite-Type $CoS_2$ Nanosheet Arrays Coated on Carbon Cloth as a Bifunctional Electrode for Overall Water Splitting. *Adv. Energy Mater.* **2018,** *8* (24), 1800935-1800947.

31. Hou, J. G.; Wu, Y. Z.; Zhang, B.; Cao, S. Y.; Li, Z. W.; Sun, L. C., Rational Design of Nanoarray Architectures for Electrocatalytic Water Splitting. *Adv. Funct. Mater.* **2019,** *29* (20), 1808367-1808406.

32. 1. Asnavandi, M.; Yin, Y.; Li, Y.; Sun, C.; Zhao, C., Promoting oxygen evolution reactions through introduction of oxygen vacancies to benchmark NiFe–OOH catalysts. ACS Energy Lett., **2018**, 3 (7), 1515-1520.

33. Huang, Z. F.; Song, J. J.; Du, Y. H.; Xi, S. B.; Dou, S.; Nsanzimana, J. M. V.; Wang, C.; Xu, Z. C. J.; Wang, X., Chemical and structural origin of lattice oxygen oxidation in Co-Zn oxyhydroxide oxygen evolution electrocatalysts. *Nat. Energy* **2019,** *4* (4), 329-338.

34. Grimaud, A.; Hong, W. T.; Shao-Horn, Y.; Tarascon, J. M., Anionic redox processes for electrochemical devices. *Nat. Mater.* **2016,** *15* (2), 121-126.

35. Zhang, X.; Xie, Y., Recent advances in free-standing two-dimensional crystals with atomic thickness: design, assembly and transfer strategies. *Chem. Soc. Rev.* **2013,** *42* (21), 8187-8199.

36. Liu, Y.; Xiao, C.; Lyu, M.; Lin, Y.; Cai, W.; Huang, P.; Tong, W.; Zou, Y.; Xie, Y., Ultrathin Co3S4 nanosheets that synergistically engineer spin states and exposed polyhedra that promote water oxidation under neutral conditions. *Angew. Chem. Int. Ed.* **2015,** *54* (38), 11231-11235.

37. Fan, H.; Huang, X.; Shang, L.; Cao, Y.; Zhao, Y.; Wu, L. Z.; Tung, C. H.; Yin, Y.; Zhang, T., Controllable Synthesis of Ultrathin Transition-Metal Hydroxide Nanosheets and their Extended Composite Nanostructures for Enhanced Catalytic Activity in the Heck Reaction. *Angew. Chem. Int. Ed.* **2016,** *55* (6), 2167-2170.

38. Wang, Y.; Zhang, Y.; Liu, Z.; Xie, C.; Feng, S.; Liu, D.; Shao, M.; Wang, S., Layered Double Hydroxide Nanosheets with Multiple Vacancies Obtained by Dry Exfoliation as Highly Efficient Oxygen Evolution Electrocatalysts. *Angew. Chem. Int. Ed.* **2017,** *56* (21), 5867-5871.

39. Raimondi, F.; Scherer, G. G.; Kotz, R.; Wokaun, A., Nanoparticles in energy technology: examples from electrochemistry and catalysis. *Angew. Chem. Int. Ed.* **2005,** *44* (15), 2190-2209.

40. Liu, S.; Yin, Y.; Ni, D. X.; Hui, K. S.; Hui, K. N.; Lee, S.; Ouyang, C. Y.; Jun, S. C., Phosphorous-containing oxygen-deficient cobalt molybdate as an advanced electrode material for supercapacitors. *Energy Storage Mater.* **2019,** *19*, 186-196.

41. Trotochaud, L.; Young, S. L.; Ranney, J. K.; Boettcher, S. W., Nickel-iron oxyhydroxide oxygen-evolution electrocatalysts: the role of intentional and incidental iron incorporation. *J. Am. Chem. Soc.* **2014,** *136* (18), 6744-6753.

42. Trzesniewski, B. J.; Diaz-Morales, O.; Vermaas, D. A.; Longo, A.; Bras, W.; Koper, M. T.; Smith, W. A., In Situ Observation of Active Oxygen Species in Fe-Containing Ni-Based Oxygen Evolution Catalysts: The Effect of pH on Electrochemical Activity. *J. Am. Chem. Soc.* **2015,** *137* (48), 15112-15121.

43. Wang, G. X.; Parrondo, J.; He, C.; Li, Y. X.; Ramani, V., Pt/C/Ni(OH)(2) Bi-Functional Electrocatalyst for Enhanced Hydrogen Evolution Reaction Activity under Alkaline Conditions. *J. Electrochem. Soc.* **2017,** *164* (13), F1307-F1315.

44. Chala, S. A.; Tsai, M. C.; Su, W. N.; Ibrahim, K. B.; Duma, A. D.; Yeh, M. H.; Wen, C. Y.; Yu, C. H.; Chan, T. S.; Dai, H.; Hwang, B. J., Site Activity and Population Engineering of NiRu-Layered Double Hydroxide Nanosheets Decorated with Silver Nanoparticles for Oxygen Evolution and Reduction Reactions. *ACS Catal.* **2019,** *9* (1), 117-129.

45. Han, J. Y.; Wang, D. P.; Du, Y. H.; Xi, S. B.; Hong, J. D.; Yin, S. M.; Chen, Z.; Zhou, T. H.; Xu, R., Metal-organic framework immobilized cobalt oxide nanoparticles for efficient photocatalytic water oxidation. *J. Mater. Chem. A* **2015,** *3* (41), 20607-20613.

46. Wong, J.; Lytle, F. W.; Messmer, R. P.; Maylotte, D. H., K-Edge Absorption-Spectra of Selected Vanadium Compounds. *Phys. Rev. B* **1984,** *30* (10), 5596-5610.

47. Giuli, G.; Paris, E.; Mungall, J.; Romano, C.; Dingwell, D., V oxidation state and coordination number in silicate glasses by XAS. *Am. Mineral.* **2004,** *89* (11-12), 1640-1646.

48. Bao, J.; Zhang, X.; Fan, B.; Zhang, J.; Zhou, M.; Yang, W.; Hu, X.; Wang, H.; Pan, B.; Xie, Y., Ultrathin Spinel-Structured Nanosheets Rich in Oxygen Deficiencies for Enhanced Electrocatalytic Water Oxidation. *Angew. Chem. Int. Ed.* **2015,** *54* (25), 7399-7404.

49. Jiang, J.; Sun, F.; Zhou, S.; Hu, W.; Zhang, H.; Dong, J.; Jiang, Z.; Zhao, J.; Li, J.; Yan, W.; Wang, M., Atomic-level insight into super-efficient electrocatalytic oxygen evolution on iron and vanadium co-doped nickel (oxy)hydroxide. *Nat. Commun.* **2018,** *9* (1), 2885-2897.

50. Zhuang, L.; Ge, L.; Yang, Y.; Li, M.; Jia, Y.; Yao, X.; Zhu, Z., Ultrathin Iron-Cobalt Oxide Nanosheets with Abundant Oxygen Vacancies for the Oxygen Evolution Reaction. *Adv. Mater.* **2017,** *29* (17), 1606793.

51. Favaro, M.; Valero-Vidal, C.; Eichhorn, J.; Toma, F.; Ross, P.; Yano, J.; Liu, Z.; Crumlin, E. J., Elucidating the alkaline oxygen evolution reaction mechanism on platinum. *J. Mater. Chem. A* **2017,** *5* (23), 11634-11643.

52. Yamamoto, K.; Imaoka, T.; Chun, W.-J.; Enoki, O.; Katoh, H.; Takenaga, M.; Sonoi, A., Size-specific catalytic activity of platinum clusters enhances oxygen reduction reactions. *Nat. Chem.* **2009**, 1 (5), 397-402.

53. Rossmeisl, J., Logadottir, A. & Nørskov, J. K. Electrolysis of water on (oxidized) metal surfaces. Chem. Phys. 319, 178–184 (2005).

54. Abild-Pedersen, F.; Greeley, J.; Studt, F.; Rossmeisl, J.; Munter, T.; Moses, P. G.; Skulason, E.; Bligaard, T.; Nørskov, J. K. Scaling properties of adsorption energies for hydrogencontaining molecules on transition-metal surfaces. Phys. Rev. Lett. 99, 016105 (2007).

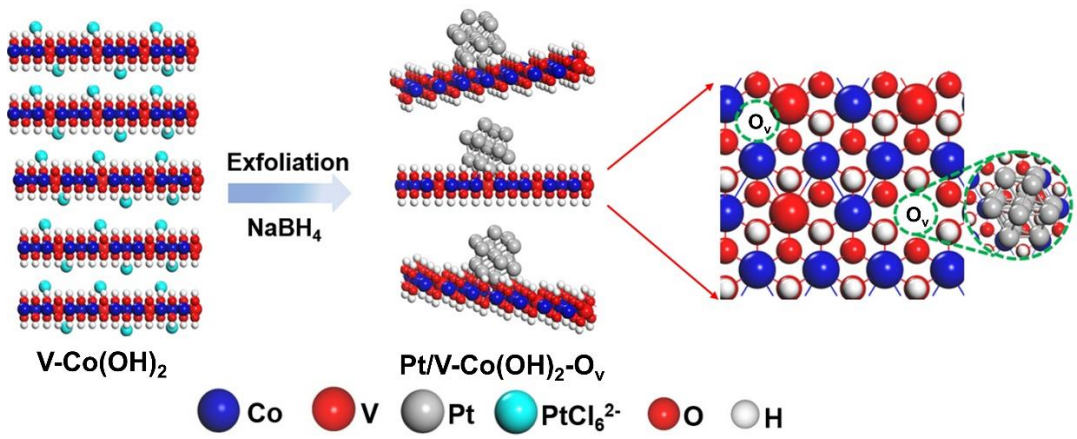


Figure 1. Schematic of the synthesis of Pt/V-Co$(OH)_2$-$O_v$ via reduction-assisted exfoliation of V-Co$(OH)_2$ by using $NaBH_4$ solution.

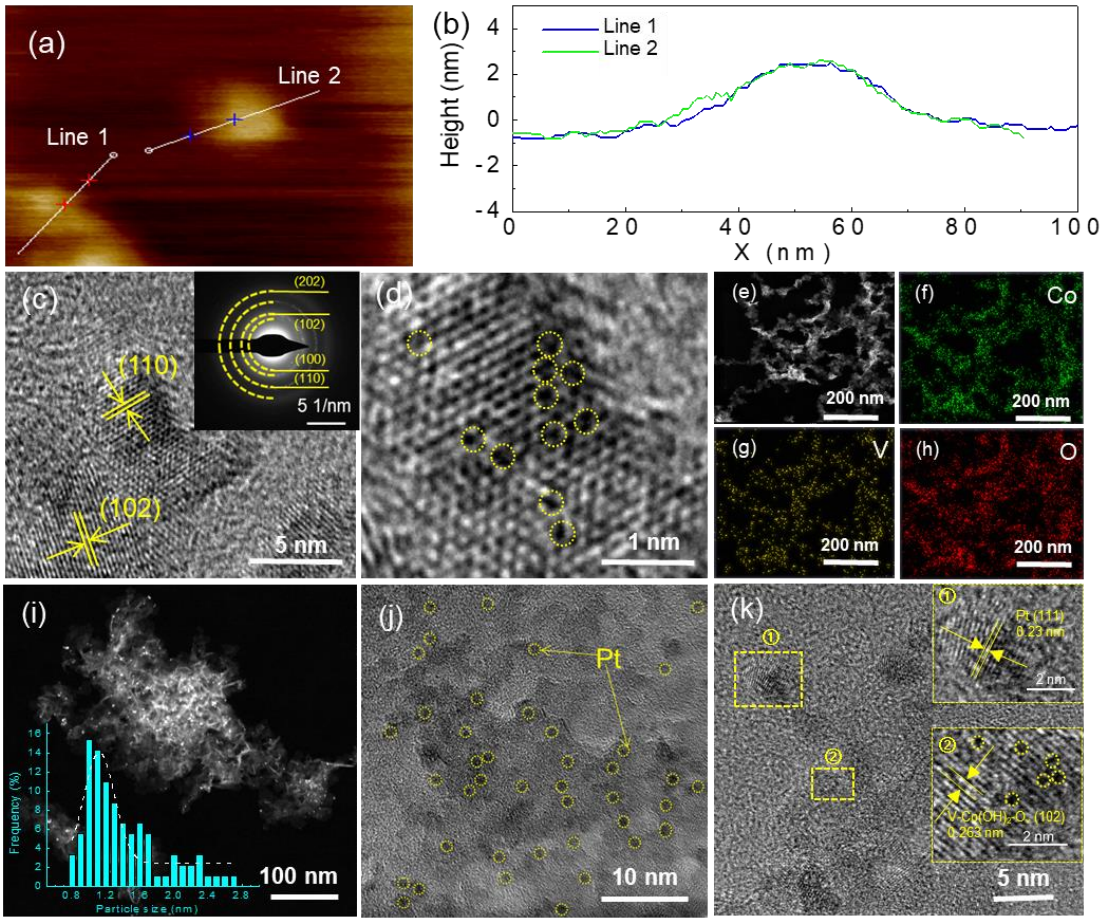


Figure 2. (a) AFM images of V-Co(OH)$_2$-O$_v$. (b) Corresponding height profiles of V-Co(OH)$_2$-O$_v$. (c) HRTEM images of V-Co(OH)$_2$-O$_v$ (inset shows the corresponding SAED images). (d) HRTEM images of V-Co(OH)$_2$-O$_v$. (e–h) HAADF-STEM images with the corresponding element distribution images of V-Co(OH)$_2$-O$_v$. (i) HAADF-STEM images of Pt/V-Co(OH)$_2$-O$_v$ (inset shows the size distribution of decorated Pt counted from the HAADF-STEM images). (j) TEM images of Pt/V-Co(OH)$_2$-O$_v$. (k) HRTEM images of Pt/V-Co(OH)$_2$-O$_v$ (inset shows the HRTEM images of Pt NPs (Zone 1) and V-Co(OH)$_2$-O$_v$ (Zone 2)).

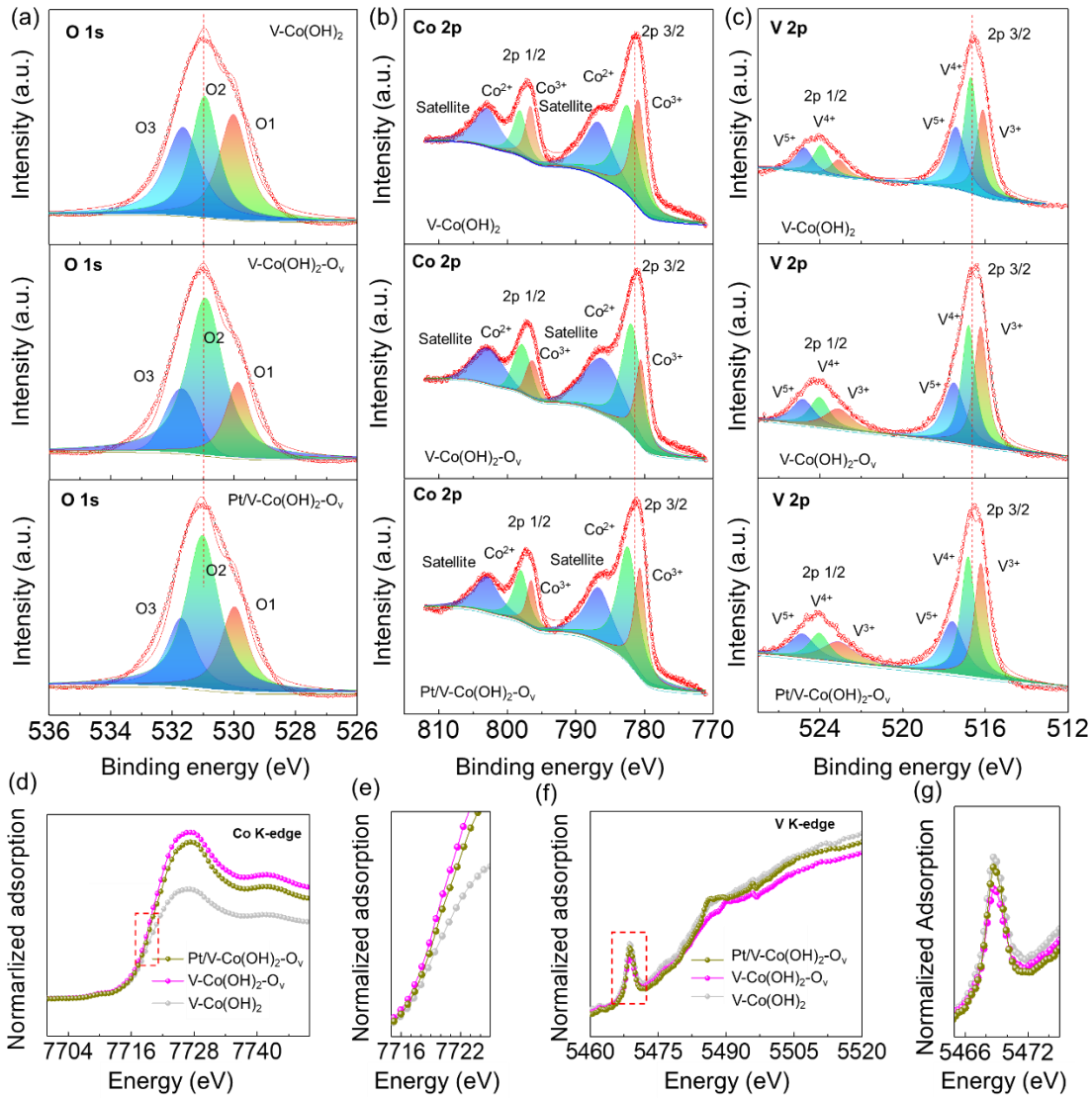


Figure 3. XPS spectra of (a) O 1s, (b) Co 2p, (c) V 2p of V-Co(OH)$_2$, V-Co(OH)$_2$-O$_v$, and Pt/V-Co(OH)$_2$-O$_v$. (d-e) Co K-edge XANES spectra for V-Co(OH)$_2$, V-Co(OH)$_2$-O$_v$, and Pt/V-Co(OH)$_2$-O$_v$. (f-g) V K-edge XANES spectra for V-Co(OH)$_2$, V-Co(OH)$_2$-O$_v$, and Pt/V-Co(OH)$_2$-O$_v$.

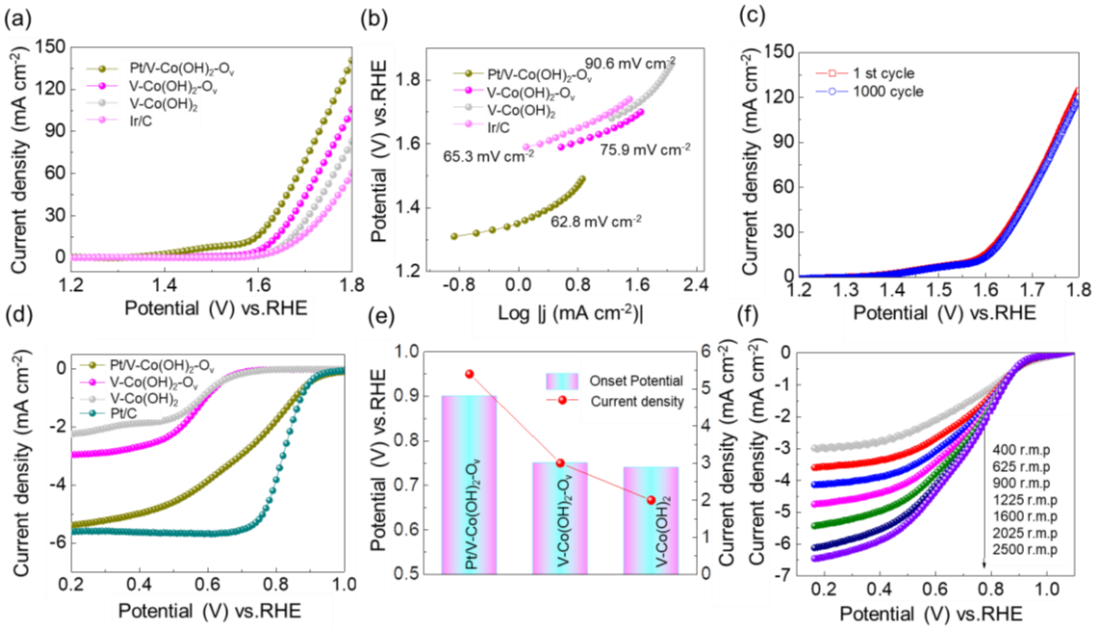


Figure 4. (a) OER polarization curves of V-Co(OH)$_2$, V-Co(OH)$_2$-O$_v$, and Pt/V-Co(OH)$_2$-O$_v$ in 1 M KOH. (b) Corresponding Tafel plots of V-Co(OH)$_2$, V-Co(OH)$_2$-O$_v$, and Pt/V-Co(OH)$_2$-O$_v$ in 1 M KOH. (c) Polarization curves of Pt/V-Co(OH)$_2$-O$_v$ before and after 1000 cycling tests. (d) ORR polarization curves of V-Co(OH)$_2$, V-Co(OH)$_2$-O$_v$, and Pt/V-Co(OH)$_2$-O$_v$ in O$_2$-saturated 0.1 M KOH. (e) Onset potentials and current densities of V-Co(OH)$_2$, V-Co(OH)$_2$-O$_v$, and Pt/V-Co(OH)$_2$-O$_v$. (f) ORR polarization curves of Pt/V-Co(OH)$_2$-O$_v$ at different rotating rates in O$_2$-saturated 0.1 M KOH.

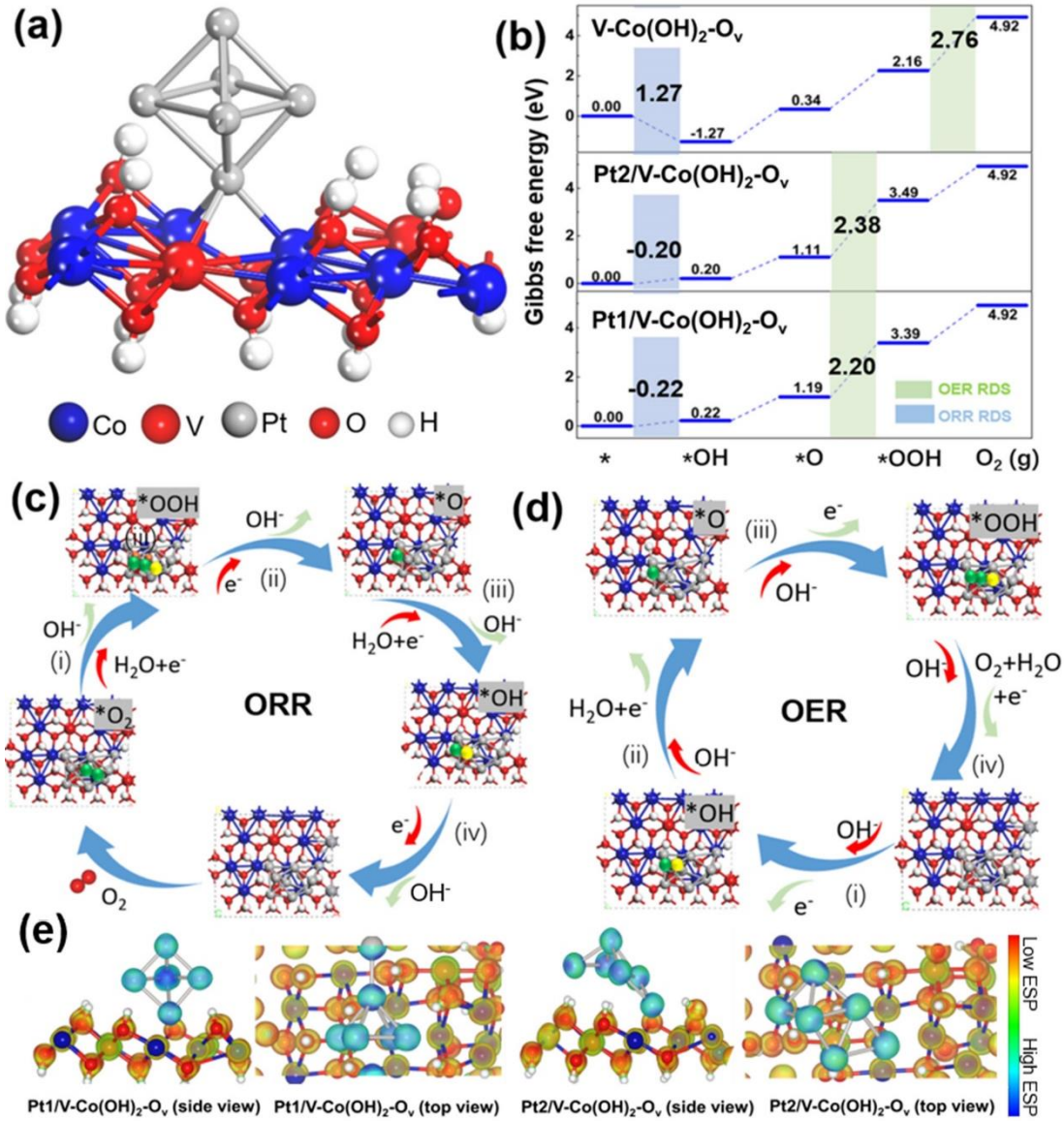


Figure 5. (a) Crystal structures of Pt1/V-Co(OH)$_2$-O$_v$ materials where Pt is anchored on the oxygen vacancy of the (102) plane of V-doped α-Co(OH)$_2$. The lattice parameters for the structure studied in this work is: a = 11.96 Å, b=6.36Å, c=25.00 Å; α=ß=γ=90°. Large blue and red balls represent the Co and V atoms, respectively. Small white and red balls represent the H and O atoms, respectively; gray balls represent the Pt NPs. (b) Primitive steps of the OER and ORR processes on the surface of V-Co(OH)$_2$-O$_v$, Pt2/V-Co(OH)$_2$-O$_v$ and Pt1/V-Co(OH)$_2$-O$_v$ (blue bar indicates ORR rate-determining step, green bar indicates OER rate-determining step). Standard free-energy diagram of (c)

ORR and (d) OER on the surface of Pt1/V-Co$(OH)_2$-$O_v$. The adsorbed oxygen and hydrogen are green and yellow balls, respectively. (e) Calculated electrostatic potential of Pt1/V-Co$(OH)_2$-$O_v$ and Pt2/V-Co$(OH)_2$-$O_v$. The reddish place has a lower electrostatic potential and is more susceptible to be attacked by electrophilic reagents. The bluer the place, the higher the electrostatic potential, and the easier it is to be attacked by nucleophilic reagents. The electron-density isosurfaces are plotted at 0.25 e $bohr^{-3}$.

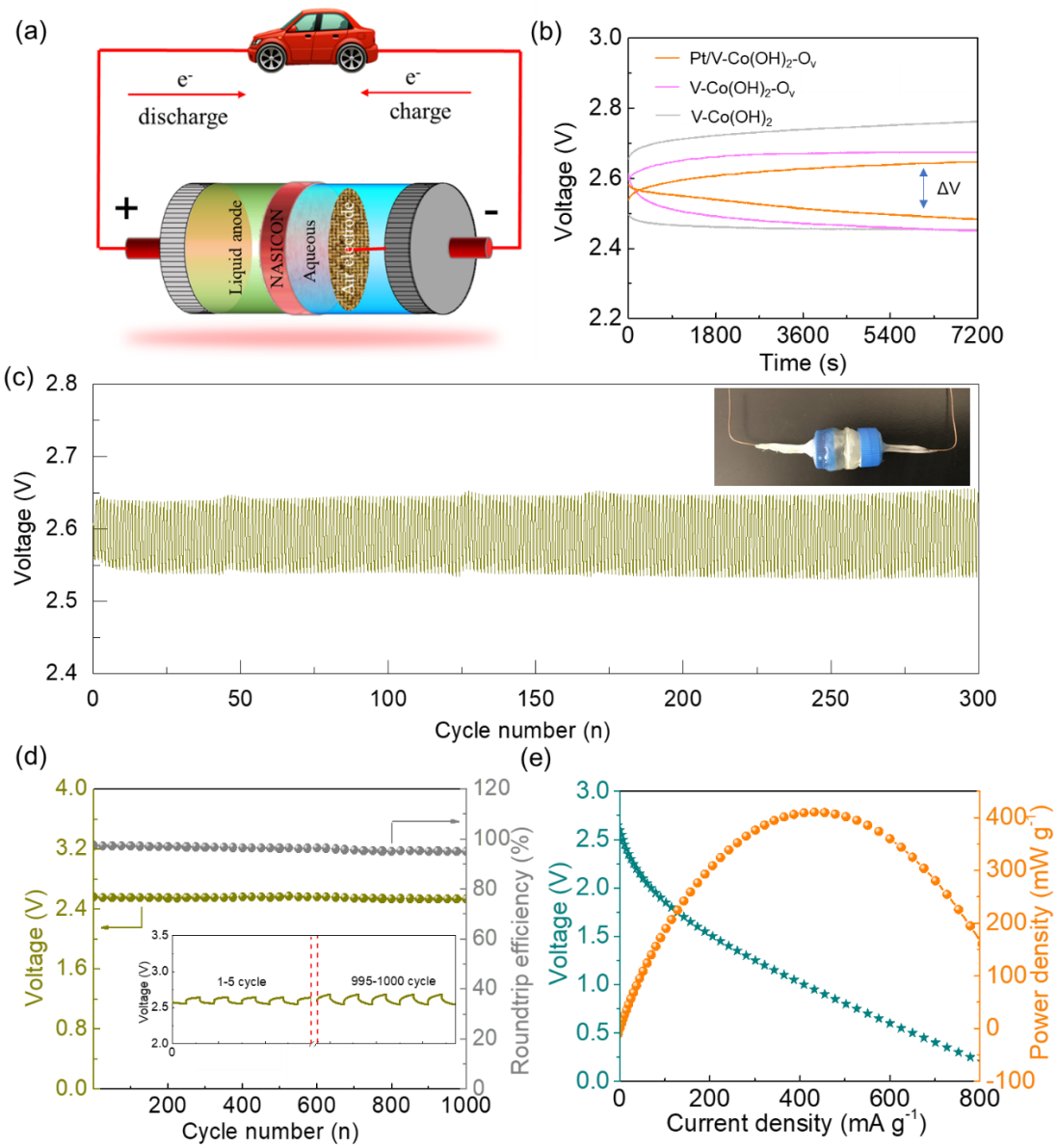


Figure 6. (a) Schematic of HSAB. (b) Charge–discharge voltage curves of the HSAB using different catalysts at the current density of 0.01 mA $cm^{-2}$. (c) Charge–discharge curves up to 300 cycles of the HSAB using Pt/V-$Co(OH)_2$-$O_v$ catalyst (20 min per-charge-discharge). (d) Roundtrip efficiency and cycling performance of the HSAB with Pt/V-$Co(OH)_2$-$O_v$ catalyst at the current density of 0.01 mA $cm^{-2}$. (e) Power density polarization of the HSAB with Pt/V-$Co(OH)_2$-$O_v$ catalyst.

Well-dispersed ultrafine platinum nanoparticles decorated on the oxygen vacancies of vanadium-doped cobalt hydroxide are fabricated by a facile and efficient method. Using the Pt/V-$Co(OH)_2$-$O_v$ as catalysts in the air cathode, a hybrid sodium–air battery displays a record value of ultralow voltage gap of 0.07 V at a current density of 0.01 mA $cm^{-2}$ with remarkable stability of up to 1000 cycles.

**Unveil the Origin of Catalytic Sites of Pt Nanoparticles Decorated on Oxygen Deficient Vanadium doped Cobalt Hydroxide Nanosheet for Hybrid Sodium–air Battery**

*Yao Kang[a,#], Shuo Wang[a,#], Yanyu Liu[b,#], Kwan San Hui[c,*], Kar Wei Ng[a], Feng Liang[d,*], Jianxin Geng[e], Xiaoting Hong[f], Wei Zhou[g,*], Kwun Nam Hui[a,*]*

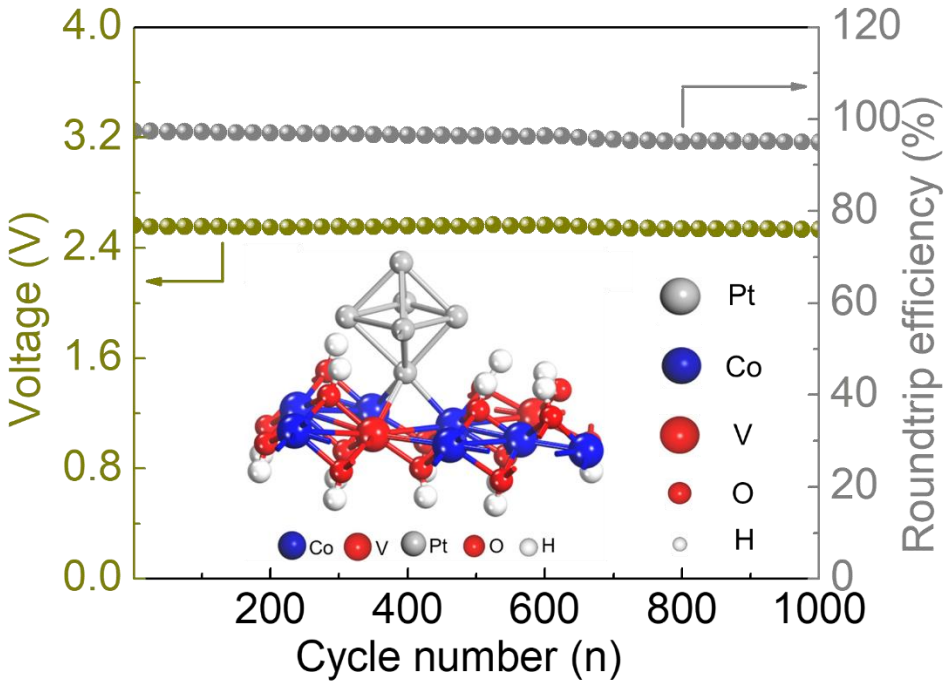


**TOC Figure**